

ELECTROMAGNETIC HEAVY ION/PROTON INSTABILITIES

Joseph J. Wang
Jet Propulsion Laboratory
Pasadena, CA 91109

S. Peter Gary
Los Alamos National Laboratory
Los Alamos, NM 87545

Paulett C. Liewer
Jet Propulsion Laboratory
Pasadena, CA 91109

21 April 1999

Abstract

Ion/ion instabilities are driven by the relative velocity v_o of two distinct ion components. This manuscript reports linear theory and simulation studies of electromagnetic ion/ion instabilities for a warm proton component streaming against a cool, heavy ion component in a homogeneous, magnetized plasma in which v_o is parallel or antiparallel to the background magnetic field. Under these conditions linear Vlasov dispersion theory predicts that the fastest growing mode is usually the right-hand polarized proton resonant instability. Two-dimensional initial value hybrid simulations of this growing mode are carried out, yielding scaling relations for the maximum fluctuating magnetic field energy density and the proton pickup time. The latter is proportional to the inverse of the maximum growth rate for a wide range of plasma parameters.

1. Introduction

There are several mechanisms by which newborn ions may interact with the plasma and magnetic fields of the solar wind. Particle/particle Coulomb collisions are relatively weak due to the low solar wind density. Two other processes operate in collisionless plasmas and are sensitive functions of α , the angle between the solar wind velocity \mathbf{v}_{sw} and the interplanetary magnetic field \mathbf{B}_o . For α values relatively close to 90° , cyclotron pickup, in which the motional electric field of the solar wind accelerates the newborn ion which then gyrates around a magnetic field line, is usually the most important pickup mechanism. If, however, α is relatively small, pickup proceeds through the relatively slower process of wave-particle interactions, as the relative streaming parallel or antiparallel to the background magnetic field of two distinct ion components can excite a variety of electromagnetic ion/ion instabilities [Gary, 1991, 1993].

Cyclotron pickup is a single-particle process which is well understood. Ion pickup by wave-particle interactions is a collective process which depends upon the various parameters of the newborn ion and solar wind plasma; although it has been the subject of many studies (e.g., Wu and Davidson [1972], Winske *et al.* [1985], Omidi and Winske [1987], Gary *et al.* [1986, 1989] and references therein), it is not yet fully understood.

Ion pickup through instability growth and wave-particle interactions may be important in a variety of different space plasmas, as indicated by observations of large-amplitude magnetic fluctuations in the environments of comets [Tsurutani *et al.*, 1997, and references therein] and the ionospheres of unmagnetized planets [Russell *et al.*, 1990]. Most previous studies of solar wind proton/heavy-ion coupling have addressed the distant cometary environment and thus have considered the case in which the solar wind protons are much more dense than the heavy ion species (e.g., water group ions). For reviews of linear theory and hybrid simulation results in this case, see, for example, Winske and Gary [1986] and Gary [1991]. Our concerns here, in contrast, are situations in which the heavy-ion density is the same order or larger than the solar wind proton density, as might be found relatively close to comets or unmagnetized planets.

Solar wind proton/heavy-ion coupling may also be relevant to plasmas introduced into the solar wind by spacecraft systems, such as the operation of an electric propulsion thruster. The 24 October 1998 launch of NASA's New Millennium Deep Space One (DS1) mission marks the beginning of interplanetary science missions using spacecraft operated on electric propulsion. All electric propulsion devices propel a spacecraft by continuously emitting a partially ionized gas, leading to an exhaust plume which is typically a relatively cool, dense, heavy ion plasma. Both science and engineering concerns have been raised over the potential effects introduced from the operation of electric propulsion devices, including whether heavy-ion/proton couplings may cause changes in the solar wind environment observed at the spacecraft.

The plume emitted from an ion thruster is composed of propellant ions, neutralizing electrons, un-ionized neutral propellant, and a charge-exchange plasma generated by collisions between propellant ions and the neutrals. The DS1 ion thruster uses xenon, which is about 140 times more massive than hydrogen, as propellant. Under typical operating conditions the xenon ions have a directed kinetic energy of about 1 keV (drift velocity about 35 km/s) and a temperature of about 0.05 eV. Both the neutralizing electrons and the charge exchange ions have a temperature of few eV. The maximum plume plasma density near the thruster exit is about 10^9 to 10^{10} cm $^{-3}$. The structure of the plume is itself not yet well understood. Studies of the plume so far have concentrated on the near-spacecraft region [Wang *et al.*, 1996]; there are no published studies regarding the global structure of the plume.

Solar wind/heavy-ion coupling related to ion thruster operation in space is a very complex problem. As the thruster ion density near the spacecraft is several orders of magnitude larger than the solar wind density, the primary physics of concern is that associated with the plume blowing a cavity in the solar wind. Sufficiently far from the plasma source where the heavy ion density has decreased to a level that the solar wind plasma and fields can penetrate the plume, the heavy ions may couple with the solar wind through collective plasma effects if α has a sufficiently small value. Even in this far-field region, effects from finite plume size may be important as the wave length of the instability is likely to be comparable to the plume size. Hence, a rigorous study of this problem requires simulations of an inhomogeneous plasma plume and needs to be treated individually for different plasma emitting devices. However, before such studies can be performed, one needs to understand first the basic properties of heavy ion/proton instabilities and scaling relations for the consequences of wave-particle interactions. This is the objective of this paper.

The research described here considers a highly idealized situation: a homogeneous plasma with solar wind protons drifting relative to a component of heavy ions. We use linear Vlasov theory (Section 3) and hybrid particle simulations (Sections 4) to study the electromagnetic heavy-ion/proton instabilities which may arise and to estimate the associated pickup rates as functions of the pertinent dimensionless parameters. Finally, we discuss the conditions which must be satisfied for the application of these results (Section 5).

2. Formulation

We consider a three component plasma: the heavy ions from the thruster denoted by subscript h , the solar wind protons denoted by sw or p as appropriate, and the electrons denoted by e . We use the subscripts \parallel and \perp to denote directions relative to \mathbf{B}_0 , the background magnetic field. We define the parallel β of the j th component or species

Table 1. Median plasma parameters in the solar wind at 1 AU
From *Gosling* [1999]

n_{sw}	v_{sw}	B_o	T_p
6.9 cm ⁻³	442 km/s	5.6 nT	8.2 eV
v_A	v_{sw}/v_A	β_p	
46 km/s	9.6	0.73	

to be $\beta_{\parallel j} \equiv 8\pi n_j k_B T_{\parallel j} / B_o^2$. We also define the cyclotron frequency of the j th species, $\Omega_j \equiv e_j B_o / m_j c$, the thermal speed of the j th species or component, $v_j \equiv \sqrt{k_B T_{\parallel j} / m_j}$, and the plasma frequency of the j th species, $\omega_j \equiv \sqrt{4\pi n_j e_j^2 / m_j}$. The Alfvén speed is defined to be that of the unperturbed solar wind plasma: $v_A = B_o / \sqrt{4\pi n_{sw} m_p}$. The average drift velocity of the j th component is denoted by \mathbf{v}_{oj} , and the relative heavy-ion/proton average drift velocity is $\mathbf{v}_o = \mathbf{v}_{op} - \mathbf{v}_{oh}$.

The character of the wave-particle interaction between a mode and a particle component or species is determined by the resonant factors which appear as arguments of the plasma dispersion function in the linear Vlasov equation [e.g., *Gary*, 1993]. At $\mathbf{k} \times \mathbf{B}_o = 0$ the cyclotron resonant factor is

$$\zeta_j^{\pm} \equiv \frac{\omega - \mathbf{k} \cdot \mathbf{v}_{oj} \pm \Omega_j}{\sqrt{2} k_{\parallel} v_j}$$

Small or intermediate values of this factor ($|\zeta| < 3$) corresponds to a resonant wave-particle interaction, whereas relatively large values such as $|\zeta| > 5$ imply that the corresponding wave-particle interaction is nonresonant or fluid-like.

The plasma is assumed to be quasineutral so $n_h + n_p = n_e$, and to carry zero current so that $n_p \mathbf{v}_{op} + n_h \mathbf{v}_{oh} - n_e \mathbf{v}_{oe} = 0$. We take both the heavy ions and the solar wind protons to be initially drifting Maxwellian distributions.

The solar wind is a tenuous, relatively hot plasma which flows radially outward from the sun. Its parameters may undergo substantial variation, but median observed values at 1 AU are listed in Table 1, as well as corresponding values for v_A , v_o/v_A , and β_p . The angle between the solar wind flow velocity \mathbf{v}_{sw} and the interplanetary magnetic field \mathbf{B}_o can vary from 0° to 90°. Since the solar wind speed is much larger than that of the heavy ions from the ion thruster, the relative drift velocity \mathbf{v}_o is dominated by the solar wind velocity.

3. Linear Theory

Table 2. Reference Parameters

Parameter	Protons	Heavy Ions	Electrons
m_j/m_p	1	140	1/1836
e_j/e_p	1.0	1.0	-1.0
n_j/n_e	n_p/n_e	$1 - n_p/n_e$	1.0
$T_{\parallel j}/T_p$	1.0	0.01	1.0
$T_{\perp j}/T_{\parallel j}$	1.0	1.0	1.0

$$v_A/c = 1 \times 10^{-4} \quad v_o/v_A = 10 \quad \beta_{\parallel p} = 1.0$$

Given two ion components moving relative to one another in a finite β plasma such as the solar wind, the strongest electromagnetic wave-particle interactions will arise when the two components move parallel or antiparallel to the background magnetic field \mathbf{B}_o [Gary *et al.*, 1989]. In this case, the maximum growth rates of the resulting ion/ion instabilities arise at $\mathbf{k} \times \mathbf{B}_o = 0$; we here consider this case, for which the linear electromagnetic Vlasov dispersion equation is well-known and is given, for example, on page 145 of Gary [1993]. We use standard numerical techniques to solve the linear dispersion equation exactly; all figures of this section display such exact results.

Table 2 shows our choice of the reference dimensionless parameters used in our solutions of the linear dispersion equation. To characterize wave-particle interactions under different situations, we perform calculations covering a range of the dimensionless parameters for proton density n_p/n_e , heavy ion mass m_h/m_p , and relative drift velocity v_o/v_A . Unless a parameter is varied or is explicitly stated to be otherwise, all calculations reported here use the values of Table 2 uniformly.

If both ion components are relatively cold protons, the two modes most likely to grow are the proton/proton right-hand resonant and the proton/proton nonresonant instabilities [Gary *et al.*, 1984]. If the more tenuous component consists of ions which are heavier than protons, Winske and Gary [1986] demonstrated that the two unstable modes have similar properties: there is a right-hand polarized growing mode which resonates with the tenuous heavy-ion component, and a heavy-ion/proton nonresonant instability. For sufficiently large values of v_o/v_A , the nonresonant instability has the larger growth rate.

Winske and Gary [1986] thoroughly addressed the linear theory scalings for the case $n_h \ll n_p$, so we here concentrate on the opposite situation, $n_p \lesssim n_h$, which is also treated to some extent by Fig. 5 of Winske and Gary [1986]. In this case as well, there are two types of modes which can grow at sufficiently large values of v_o/v_A . One mode, which we call the "proton resonant instability," has right-hand polarization and near maximum

growth rate approximately satisfies the proton cyclotron resonance condition,

$$\omega_r - \mathbf{k} \cdot \mathbf{v}_o \pm \Omega_p = 0 \quad (1)$$

so that typically $|\zeta_p^\pm| \lesssim 1$. The second type of mode usually corresponds to left-hand polarization and resonates with the more dense heavy ion component so that $|\zeta_h^\pm| \lesssim 1$ for many wavenumbers of fluctuation growth. Under many conditions there are two distinct such modes with similar growth rates but opposite helicities; we term these "heavy-ion resonant instabilities."

Figure 1 illustrates the maximum growth rate and the corresponding wavenumber of both types of instabilities as functions of the ratio of the proton (that is, solar wind) density to the density of the heavy ions. For the parameters of Table 2, the maximum growth rates of the heavy-ion resonant instabilities are relatively independent of n_p/n_e , and are much smaller than that of the proton resonant instability. Figure 1 also shows that for the proton resonant instability the domain of fastest growth rate is $0.50 \lesssim n_p/n_e \lesssim 0.80$ and the domain of largest wavenumbers is $0.65 < n_p/n_e < 0.90$. The plasma clouds from spacecraft ion propulsion systems will be relatively limited in spatial extent, so it will be the shortest wavelength, fastest growing instabilities which have the greatest potential for scattering ions.

Figure 2 illustrates the maximum growth rates and the corresponding wavenumbers of these instabilities as functions of the dimensionless heavy-ion/proton relative drift speed. For the dimensionless parameters of Table 2, the proton resonant instability has the largest growth rate for all drift speeds of interest. It is also clear that, for $v_o \gg v_A$, the maximum growth rate of the heavy-ion resonant instabilities are essentially independent of v_o/v_A .

Figure 3 shows the maximum growth rate and the corresponding wavenumber of these instabilities as functions of the heavy-ion/proton mass ratio. Here γ_m/Ω_p of the proton resonant mode is a relatively weak function of the mass ratio of the two ion components, but the maximum growth rates of the heavy-ion resonant modes are roughly proportional to m_p/m_h so that the former mode dominates in the limit of large m_h/m_p . Figure 3 shows that, for the parameters of Table 2, computer simulations of the proton resonant instability with $m_h/m_p \simeq 16$ should display the same linear properties as simulations of this instability at much larger mass ratios.

We have not found an appropriate expansion of the plasma dispersion function for the proton contribution to the linear dispersion of the proton resonant instability, and we have not obtained a simple analytic expression for γ_m/Ω_p of this mode. From the proton resonant condition Equation (1), at $n_p \ll n_e$ where $\omega_r \ll \Omega_p$,

$$\frac{kc}{\omega_p} \simeq \frac{v_A}{v_o} \quad (2)$$

Figures 1b, 2b, and 3b confirm that this is indeed an appropriate scaling for $n_p \ll n_e$.

On the other hand if one considers the more persistent heavy-ion resonant instability and chooses wavenumbers somewhat away from maximum growth, all three components are nonresonant, and the cold plasma approximation may be used for each term. Our numerical solution shows that the imaginary parts of the heavy-ion and electron terms are approximately equal and opposite, so equating the cold plasma limits of these two, using $n_p \ll n_e$, and invoking the empirical result $\omega_r \simeq \Omega_h$ we obtain

$$\frac{\gamma_m}{\Omega_p} \simeq \frac{m_p}{m_h} \quad (3)$$

which well describes the appropriate limiting cases for the heavy-ion resonant instabilities in Figures 1a, 2a, and 3a.

There is one more linear theory result which is useful in the preparation of our simulations. Figure 4 shows the maximum growth rate for the proton resonant instability as a function of θ for representative parameters. The important result here is that this instability (as well as the heavy-ion resonant instabilities which are not shown) remains strongly unstable out to very oblique directions of propagation relative to \mathbf{B}_o . This result suggests that oblique wave propagation is very important in this case and hence, two-dimensional simulations may be more appropriate than previous one-dimensional simulations of electromagnetic heavy-ion/proton instabilities. Moreover, this result also implies that in two-dimensional simulations same grid resolution should be used in the directions perpendicular to and parallel to \mathbf{B}_o .

4. Simulations

This section describes results from computer simulations of electromagnetic heavy-ion/proton instabilities. We have used a two-dimensional hybrid code that treats the ions as discrete particles and the electrons as a massless fluid [Winske and Omidi, 1993]. The one-dimensional version of this code has been used in many previous studies of electromagnetic ion/ion instabilities [Winske and Leroy, 1984; Omidi and Winske, 1987; Gary *et al.*, 1986, 1989]. This two-dimensional hybrid code was recently used to simulate electromagnetic proton cyclotron and mirror [Gary *et al.*, 1997] as well as proton/proton [Daughton *et al.*, 1999] instabilities.

The simulations are performed in the center of mass frame. At $t = 0$, the proton and heavy ion components, each assumed to be a drifting Maxwellian distribution, stream parallel to \mathbf{B}_o with a relative speed v_o . Based on the results of Figure 4, the simulations are carried out in systems with equal dimensions parallel and perpendicular to \mathbf{B}_o and with the same spatial resolution in these two directions. Both the grid resolution and domain length are adjusted according to the wave numbers calculated from the linear theory in

Section 3 so both the proton resonant modes and heavy-ion resonant modes can be resolved in the simulation. On average, about 100 particles per cell are used for each ion component and about one million test particles are used in a typical run.

We first describe detailed results from a representative simulation. We then discuss the scaling relations obtained from several ensembles of simulations corresponding to a range of values of n_p/n_e , v_o/v_A , and m_h/m_p .

Our representative simulation addressed a plasma in which the heavy ions were the more dense component, with $n_p/n_e = 0.1$. Three different initial drift velocities are considered: $v_o/v_A = 10$, 4 and 2. Other initial parameters are as stated in Table 2. For simulations of each initial drift velocity, we used a 64×64 computational grid with the simulation system length ($L_{\parallel} = L_{\perp}$) chosen to be about 7.6 to 8.2 times the wavelength of the proton resonant mode, which also corresponds to a little more than twice of the wavelength of the heavy-ion resonant mode for that drift velocity. Hence, both the proton resonant and heavy ion resonant modes can be resolved in the simulation. The integration time step is $\Omega_p \Delta t = 0.125$.

Figure 5 illustrates the fluctuating magnetic field energy density and the average heavy-ion/proton relative drift as functions of time. For the $v_o/v_A = 10$ case, the fluctuating magnetic fields exhibit an exponential temporal growth at early times ($\Omega_p t \lesssim 35$), and a more gradual temporal growth at later times to $|\delta B|^2/B_o^2 \simeq 0.33$ at $\Omega_p t \simeq 300$. Wave-particle scattering is relatively weak during the initial exponential temporal growth phase, but starts to assert itself strongly at the end of the exponential growth phase, reducing the relative drift velocity to zero. On the other hand, for the $v_o/v_A = 4$ and 2 cases, the fluctuating magnetic fields exhibit only exponential growth followed by a more gradual decrease in energy density.

To identify the dominant mode in the simulations, we have compared the growth rate and wave number obtained from the simulation with that from linear theory. Figure 6 shows the early stage of the instability and a snapshot of the power spectrum $B_{\perp}(k_x, k_y)$ at $\Omega_p t = 37.5$ for the $v_o/v_A = 10$ case. Linear theory predicts that maximum growth rates and corresponding wavenumbers for $n_p/n_e = 0.1$ and $v_o/v_A = 10$ are $\gamma_m/\Omega_p = 0.3$ and $k_m c/\omega_p = 0.12$ for the proton resonant instability and $\gamma_m/\Omega_p = 0.0076$ and $k_m c/\omega_p = 0.0297$ for the heavy-ion resonant instability, respectively. In the simulation, the growth rate during the period of exponential growth is $\gamma/\Omega_p \simeq 0.28$. The simulation system length for this case is $L_{\parallel} = L_{\perp} \simeq 425c/\omega_p$. The power spectrum is dominated by the mode $(k_x, k_y) = (8, 0)$, corresponding to a wavenumber of $kc/\omega_p \simeq 0.12$. Comparing with the results from the linear theory, we conclude that the dominant mode in this simulation is the proton resonant instability. We obtained the same conclusion for the two other representative simulations as well.

Figures 7 and 8 show sequences of phase space snapshots for the protons and the

heavy ions, respectively, in the $v_o/v_A = 10$ simulation. The primary consequence of wave-particle scattering by enhanced fluctuations from the resonant instability is pitch-angle scattering of the resonant component [Winske and Leroy, 1984; Winske and Gary, 1986]. The protons are first scattered toward a thin velocity-space shell of radius approximately equal to the initial value of v_o , and then eventually into a spherical velocity distribution. The parallel streaming energy of the protons is primarily transferred to perpendicular energy via pitch angle scattering. A small part of the proton energy appears in the field fluctuations and the heavy ions. These results are similar to previous one-dimensional results [Winske and Leroy, 1984]. While the proton momentum goes primarily into the heavy ions, the parallel velocity distribution of the heavy ions stays relatively unchanged throughout the simulation due to their heavy mass. Hence, the protons are picked up by the heavy ions and eventually become isotropized in the center of the mass frame. For comparison, Figure 9 shows proton and heavy ion phase space plots after instability saturation for the $v_o/v_A = 2$ case. Due to the smaller initial free energy, the magnetic field fluctuation from the proton resonant instability is at much lower level. As a result, the protons are only scattered into a kidney-shaped distribution and are only partially picked up by the heavy ions.

In previous simulations of cool heavy ion beams streaming against a proton core, the core distribution typically remains unchanged during beam-resonant interactions. However, as Figure 8 shows, here the heavy ion core exhibits substantial heating in the perpendicular direction. We find that such perpendicular heating of the core only occurs for relatively large initial drift velocities. For instance, for $n_p/n_e = 0.1$, perpendicular heating of the heavy ions occurs for $v_o/v_A \gtrsim 5$. Figure 10 shows the change of the total energy and the temperature anisotropy for the heavy ion component as a function of time. Here the temperature is defined as the second moment of the distribution function. While at lower drift velocities (e.g. $v_o/v_A = 2$), the free energy lost by the proton component mainly goes to the magnetic fluctuations, the heavy ions become a more significant sink for the free energy at higher drift velocities. Comparing Figure 10a and Figure 5a, it's clear that at $v_o/v_A = 10$, the energy acquired by the heavy ions far exceeds that gained by the magnetic fluctuations. Corresponding to the perpendicular heating of the heavy ion component, the magnetic field energy density changes from the initial exponential growth to a more gradual temporal growth.

This suggests that one may categorize heavy ion/proton instabilities as weakly driven or strongly driven. In the weakly driven cases, the heavy-ion component remains relatively isotropic and the magnetic fluctuations receives most of the energy lost by the protons. But in the more strongly driven cases, the heavy ions as well as the magnetic fluctuations become a sink for free energy lost by the proton component, corresponding to a comparatively lower level of field energy than in the more weakly driven cases in which

only $|\delta B|^2/8\pi$ receives energy lost by the protons. A signature for the strongly driven interactions is that the heavy-ion component shows a strong temperature anisotropy such that $T_{\perp h}/T_{\parallel h} > 1$.

We next carried out several ensembles of simulations to address scaling relations for the maximum fluctuating field energy density and the proton pickup time. Previous studies of electromagnetic ion/ion instabilities [Gary *et al.*, 1986; Winske and Gary, 1986] indicate a maximum fluctuating field energy density at $n_1 \ll n_e$ which scales as

$$\frac{|\delta B|^2}{B_o^2} \simeq \frac{S_B}{2} \frac{n_1}{n_e} \left(\frac{v_o}{v_A} \right)^2 \quad (4)$$

where subscript 1 indicates the more tenuous ion component. In general S_B is a function of mass; if both components are protons, $S_B = 1$, but in the more general case we assume the form $(m_1/m_2)^{\alpha_m}$. Although the proton velocity distribution becomes non-Maxwellian as a result of wave-particle interactions, the average relative drift speed, v_o , remains a well-defined quantity. As in Figure 5, v_o exhibits an exponential-like decrease in time for each simulation of our ensembles, so it is appropriate to define the pickup time τ_p to be the e-folding decay time for v_o . Furthermore, we expect that $\tau_p \Omega_p$ may be inversely proportional to the maximum growth rate, so we define S_τ by

$$\tau_p \Omega_p = S_\tau \frac{\Omega_p}{\gamma_m} \quad (5)$$

and seek to determine the properties of this fitting parameter by comparison against the results of the simulation ensembles.

Figure 11 illustrates results for an ensemble of simulations using the initial conditions of Table 2 and the following values of the relative proton density: $n_p/n_e = 0.01, 0.02, 0.05, 0.1, 0.2, 0.3, 0.4$, and 0.5 . This figure shows that the dimensionless magnetic fluctuation energy density increases with proton density approximately as in Equation (4) with $S_B = (m_p/m_h)^{1/2}$.

Figure 12 illustrates results obtained from an ensemble of simulations in which $n_p/n_e = 0.10$, the initial values of the heavy-ion/proton relative drift speed are $v_o/v_A = 1.5, 2.0, 4.0, 6.0, 10.0$ and 20.0 , and all other initial values are as given in Table 2. This figure shows the dimensionless fluctuating magnetic field energy density as a function of v_o/v_A ; for comparison Equation (4) with $S_B = (m_p/m_h)^{1/2}$ is also presented. At $v_o/v_A \leq 2$, the enhanced fluctuations do not scatter the protons strongly enough to yield an e-folding reduction in the relative drift of the two ion components. In contrast, over $6 \leq v_o/v_A \leq 20$, the pickup time is approximately constant at $\tau \Omega_p \simeq 42$; as $\gamma_m \simeq 0.3$ from Figure 2a, $S_\tau \simeq 4\pi$.

Figure 13 illustrates results obtained from an ensemble of simulations in which $n_p/n_e = 0.10$, the initial values of the heavy-ion/proton mass ratio are $m_h/m_p = 20$,

60, 100, and 140.0, and all other initial values are as given in Table 2. The scalings from *Gary et al.* [1986] and *Winske and Gary* [1986] are not useful here, as they address instabilities in which the more tenuous component is of equal mass or heavier than the more dense component. The proton pickup time is essentially constant at $\tau\Omega_p \simeq 41$ for the four simulations of this ensemble; as the maximum growth rate of the proton resonant instability illustrated in Figure 3a is also essentially constant for this domain of m_h/m_p , we once again obtain $S_\tau \simeq 4\pi$. In contrast Figure 13 shows that the fluctuating magnetic field energy density increases as m_h/m_p decreases; once again Equation (4) provides a fairly good fit to the simulation results with $S_B = (m_p/m_h)^{1/2}$.

We summarize results for the maximum value of the fluctuating magnetic field energy density from four different ensembles of simulations in Figure 14, which illustrates $|\delta B|^2/B_o^2$ as a function of $1/2(m_p/m_h)^{1/2}n_p/n_h(v_o/v_A)^2$ where v_o is the heavy-ion/proton relative drift speed at the initiation of each simulation. The four ensembles are the three corresponding to Figures 11, 12, and 13, and one in which $n_p/n_e = 0.01$, $m_h/m_p = 140$ and v_o/v_A is varied. At $1/2(m_p/m_h)^{1/2}n_p/n_h(v_o/v_A)^2 \gtrsim 0.2$, our results fall into the strongly driven category which correspond to Equation (4) with $S_B \simeq (m_p/m_h)^{1/2}$. Whereas at $1/2(m_p/m_h)^{1/2}n_p/n_h(v_o/v_A)^2 \lesssim 0.05$, our results fall into the weakly driven category which correspond to Equation (4) with $S_B \simeq (m_p/m_h)^{1/4}$. The transition from the weakly driven interactions at lower free energy to strongly driven interactions at higher free energy is obvious in Figure 14.

Results for the proton pickup time from these same ensembles are summarized in Figure 15; here $\tau_p\gamma_m$ is plotted as a function of $1/2(m_p/m_h)^{1/2}n_p/n_h(v_o/v_A)^2$ where v_o is the heavy-ion/proton relative drift speed at $t = 0$. For the ensembles considered here, $\tau_p\Omega_p$ varies by two orders of magnitude whereas, as Figure 15 shows, the product $\tau_p\gamma_m$ exhibits much less variation and is therefore a useful quantity to consider. At relatively weak free energy, $\tau_p\gamma_m$ becomes large, corresponding to the inability of the instability to scatter the protons to isotropy at weak but nonzero growth. As the free energy increases, $\tau_p\gamma_m$ approaches a lower bound of about 10; in other words, the proton pickup time is inversely proportional to the maximum growth rate for strongly driven cases.

5. Conclusions

We have used linear Vlasov theory and two-dimensional hybrid simulations to study the properties of electromagnetic heavy-ion/proton instabilities in homogeneous plasmas. Linear theory predicts the growth of the proton resonant right-hand mode and two left-hand heavy-ion resonant instabilities. The latter modes have maximum growth rates which scale inversely as the heavy-ion mass, so we expect the former mode to be more important under a wide domain of conditions, and our simulations confirm this expectation. The simulations also confirm previous results from one-dimensional hybrid simulations that the

largest fluctuating magnetic field energy densities correspond to the fastest linear growth rates; that is, when the proton and heavy-ion components have similar densities.

New results presented here include linear theory scalings for the instability wavenumbers at maximum growth and scaling relations derived from the simulations for the maximum fluctuating field amplitude and the proton pickup rate. If the proton resonant instability is driven relatively strongly, the maximum $|\delta B|^2/B_o^2$ is proportional to $(m_p/m_h)^{1/2}$ and the proton pickup time is inversely proportional to the maximum growth rate.

Our results provide new insights into the general problem of heavy-ion/proton instabilities. However, the application of these results are constrained to physical situations in which the various assumptions of the theory are satisfied. The assumption of a spatially homogeneous plasma in particular imposes two requirements.

The WKB condition for validity of the spatially homogeneous theory is that the wavelength of the fluctuation should be short compared to gradients in the background plasma; this translates into the condition

$$2\pi \frac{|dn/dx|}{n(x)} \ll k$$

Hence, application of our results are limited to plasma regions that satisfy this condition.

In addition if the plasma is limited in spatial extent to, say, L_\perp (as it clearly will be in the case of an ion propulsion plume), the wavevector component in this direction must be large enough to permit the growing mode to “fit,” i.e.

$$k_\perp L_\perp \gtrsim 2\pi$$

Another limiting assumption is the requirement that α , the angle between the solar wind flow velocity and \mathbf{B}_o , be sufficiently small to excite the ion/ion instabilities considered here. As this angle increases, the heavy-ion/proton relative drift decreases and the growth rate of the associated instability decreases. Figure 2 suggests that the proton resonant instability should generally have significant growth as long as

$$\frac{v_o}{v_A} \cos \alpha \gtrsim 1$$

As α approaches 90° , the newborn ion distribution becomes more ringlike, and the fastest growing electromagnetic instability becomes the left-hand polarized ion anisotropy mode which has been studied in the newborn ion context by *Gary et al.* [1989] and *Gray et al.* [1996].

Acknowledgments. The work at Jet Propulsion Laboratory, California Institute of Technology, was performed under a contract with NASA. Access to the Cray supercomputer

used in this study was provided by funding from NASA Offices of Aeronautics, Mission to Planet Earth, and Space Science. The Los Alamos portion of this work was performed under the auspices of the U.S. Department of Energy (DOE) and was supported by the DOE Office of Basic Energy Sciences, Division of Engineering and Geosciences, and the National Aeronautics and Space Administration.

References

- Daughton, W. S., S. P. Gary, and D. Winske, Electromagnetic proton/proton instabilities in the solar wind: simulations, *J. Geophys. Res.*, *104*, 4657, 1999.
- Gary, S. P., Electromagnetic ion/ion instabilities and their consequences in space plasmas: A review, *Space Sci. Revs.*, *56*, 373, 1991.
- Gary, S. P., *Theory of Space Plasma Microinstabilities*, Cambridge University Press, Cambridge, 1993.
- Gary, S. P., C. W. Smith, M. A. Lee, M. L. Goldstein, and D. W. Forslund, Electromagnetic ion beam instabilities, *Phys. Fluids*, *27*, 1852, 1984.
- Gary, S. P., C. D. Madland, D. Schriver, and D. Winske, Computer simulations of electromagnetic cool ion beam instabilities, *J. Geophys. Res.*, *91*, 4188, 1986.
- Gary, S. P., K. Akimoto, and D. Winske, Computer simulations of cometary-ion/ion instabilities and wave growth, *J. Geophys. Res.*, *94*, 3513, 1989.
- Gary, S.P., J. Wang, D. Winske, and S. Fuselier, Proton temperature anisotropy upper bound, *J. Geophys. Res.*, *102*, 27159, 1997.
- Gosling, J. T., The solar wind, *Encyclopedia of the Solar System*, Academic Press, 1999.
- Gray, P. C., C. W. Smith, W. H. Matthaeus, and N. F. Otani, Heating of the solar wind by pickup ion driven Alfvén ion cyclotron instability, *Geophys. Res. Lett.*, *23*, 113, 1996.
- Omidi, N., and D. Winske, A kinetic study of solar wind mass loading and cometary bow shocks, *J. Geophys. Res.*, *92*, 13,409, 1987.
- Russell, C. T., J. G. Luhmann, K. Schwingenschuh, W. Riedler, and Ye. Yeroshenko, Upstream waves at Mars: Phobos observations, *Geophys. Res. Lett.*, *17*, 897, 1990.
- Tsurutani, B. T., G. S. Lakhina, F. M. Neubauer, and K.-H. Glassmeier, A new look at the nature of comet Halley's LF electromagnetic waves: Giotto observations, *Geophys. Res. Lett.*, *24*, 3129, 1997.
- Wang, J., J. Brophy, and D. Brinza, 3-D simulations of NSTAR ion thruster plasma environment, *AIAA 96-3202*, 1996.
- Winske, D., and S. P. Gary, Electromagnetic instabilities driven by cool heavy ion beams, *J. Geophys. Res.*, *91*, 6825, 1986.

Winske, D. and N. Omid, Hybrid codes, methods and applications, in *Computer Space Plasma Physics: Simulation Techniques and Software*, edited by H. Matsumoto and Y. Omura, Tokyo, 1993.

Winske, D., C. S. Wu, Y. Y. Li, Z. Z. Mou, and S. Y. Guo, Coupling of newborn ions to the solar wind by electromagnetic instabilities and their interaction with the bow shock, *J. Geophys. Res.*, **90**, 2713, 1985.

Wu, C. S., and R. C. Davidson, Electromagnetic instabilities produced by neutral particle ionization in interplanetary space, *J. Geophys. Res.*, **77**, 5399, 1972.

Figure Captions

Figure 1. Linear theory results: (a) maximum growth rates and (b) wavenumbers at maximum growth rate of the proton resonant instability (solid line) and heavy-ion resonant instability (dashed line) as functions of the relative density of the proton beam. Dimensionless parameters are as given in Table 2.

Figure 2. Linear theory results: (a) maximum growth rates and (b) wavenumbers at maximum growth rate of the proton resonant instability (solid line) and heavy-ion resonant instability (dashed line) as functions of the dimensionless heavy-ion/proton relative drift speed. Dimensionless parameters are as given in Table 2 with $n_p/n_e = 0.10$.

Figure 3. Linear theory results: (a) maximum growth rates and (b) wavenumbers at maximum growth rate of the proton resonant instability (solid line) and heavy-ion resonant instability (dashed line) as functions of the heavy-ion/proton mass ratio. Dimensionless parameters are as given in Table 2 with $n_p/n_e = 0.10$ and m_h/m_p variable.

Figure 4. Linear theory results: The growth rate of the proton resonant instability maximized over wavenumber as a function of the angle of propagation relative to the background magnetic field. Dimensionless parameters are as given in Table 2 with $n_p/n_e = 0.10$; the three curves correspond to the three indicated values of v_o/v_A .

Figure 5. Representative simulation results: (a) The fluctuating magnetic field energy density and (b) the average heavy-ion/proton relative drift speed as functions of time. Initial parameters are as given in Table 2 $n_p/n_e = 0.1$, and $v_o/v_A = 10$ (solid line), 4 (dashed line), and 2 (dotted line).

Figure 6. Representative simulation results: (a) early time evolution of the fluctuating magnetic field energy density and (b) the power spectrum of $B_\perp(k_x, k_y)$ at $\Omega_p t = 37.5$. $n_p/n_e = 0.1$ and $v_o/v_A = 10$. Initial parameters are as given in Table 2 with $n_p/n_e = 0.1$.

Figure 7. Representative simulation results: Proton velocity space plots at (a) $\Omega_p t = 0$, (b) $\Omega_p t = 37.5$, (c) $\Omega_p t = 75$, and (d) $\Omega_p t = 250$. Initial parameters are as given in Table 2 with $n_p/n_e = 0.1$ and $v_o/v_A = 10$.

Figure 8. Representative simulation results: Heavy ion velocity space plots at (a) $\Omega_p t = 0$, (b) $\Omega_p t = 75$, (c) $\Omega_p t = 250$, and (d) $\Omega_p t = 500$. Initial parameters are as given in Table 2 with $n_p/n_e = 0.1$ and $v_o/v_A = 10$.

Figure 9. Representative simulation results: The proton velocity space plots (a) and the heavy ion velocity space plots (b) at $\Omega_p t = 250$. Initial parameters are as given in Table 2 with $n_p/n_e = 0.1$ and $v_o/v_A = 2$.

Figure 10. Representative simulation results: The temporal evolution of the energy change $\delta n_h m_h v_h^2$ (a) and the temperature anisotropy $T_{\perp h}/T_{\parallel h}$ (b) for the heavy ion component. Initial parameters are as given in Table 2 $n_p/n_e = 0.1$, and $v_o/v_A = 10$ (solid line), 4 (dashed line), and 2 (dotted line).

Figure 11. Simulation ensemble results: The maximum fluctuating magnetic field energy density as a function of n_p/n_e is shown as solid triangles. Initial parameters are as given in Table 2. The dashed line represents Equation (4) with $S_B = (m_p/m_h)^{1/2}$.

Figure 12. Simulation ensemble results: The maximum fluctuating magnetic field energy density as a function of v_o/v_A is shown as dots. Initial parameters (except for v_o/v_A) are as given in Table 2 with $n_p/n_e = 0.10$. The dashed line represents Equation (4) with $S_B = (m_p/m_h)^{1/2}$.

Figure 13. Simulation ensemble results: The maximum fluctuating magnetic field energy density as a function of m_h/m_p is shown as solid diamonds. Initial parameters (except for m_h/m_p) are as given in Table 2 with $n_p/n_e = 0.10$. The dashed line represents Equation (4) with $S_B = (m_p/m_h)^{1/2}$.

Figure 14. Simulation ensemble results: The maximum fluctuating magnetic field energy density as a function of $1/2(m_p/m_h)^{1/2} n_p/n_h (v_o/v_A)^2$ where v_o/v_A is the dimensionless heavy-ion/proton relative drift speed at $t = 0$ of each simulation. The solid triangles represent results from the ensemble corresponding to Figure 11 (variable n_p/n_h); the solid dots represent results from the ensemble corresponding to Figure 12 ($n_p/n_e = 0.10$ and variable v_o/v_A); the solid diamonds represent results from the ensemble corresponding to Figure 13 ($n_p/n_e = 0.10$ and variable m_h/m_p); and the open circles correspond to an ensemble with $n_p/n_e = 0.01$, $m_h/m_p = 140$, and variable v_o/v_A . The dashed lines represent Equation (4) with $S_B = (m_p/m_h)^{1/4}$ (the upper line) and $S_B = (m_p/m_h)^{1/2}$.

Figure 15. Simulation ensemble results: The product of the proton pickup time and the maximum growth rate of the proton resonant instability as a function of $1/2(m_p/m_h)^{1/2} n_p/n_h (v_o/v_A)^2$ where v_o/v_A is the dimensionless heavy-ion/proton relative drift speed at $t = 0$ of each simulation. The symbols correspond to the same ensembles as described in the caption of Figure 14.

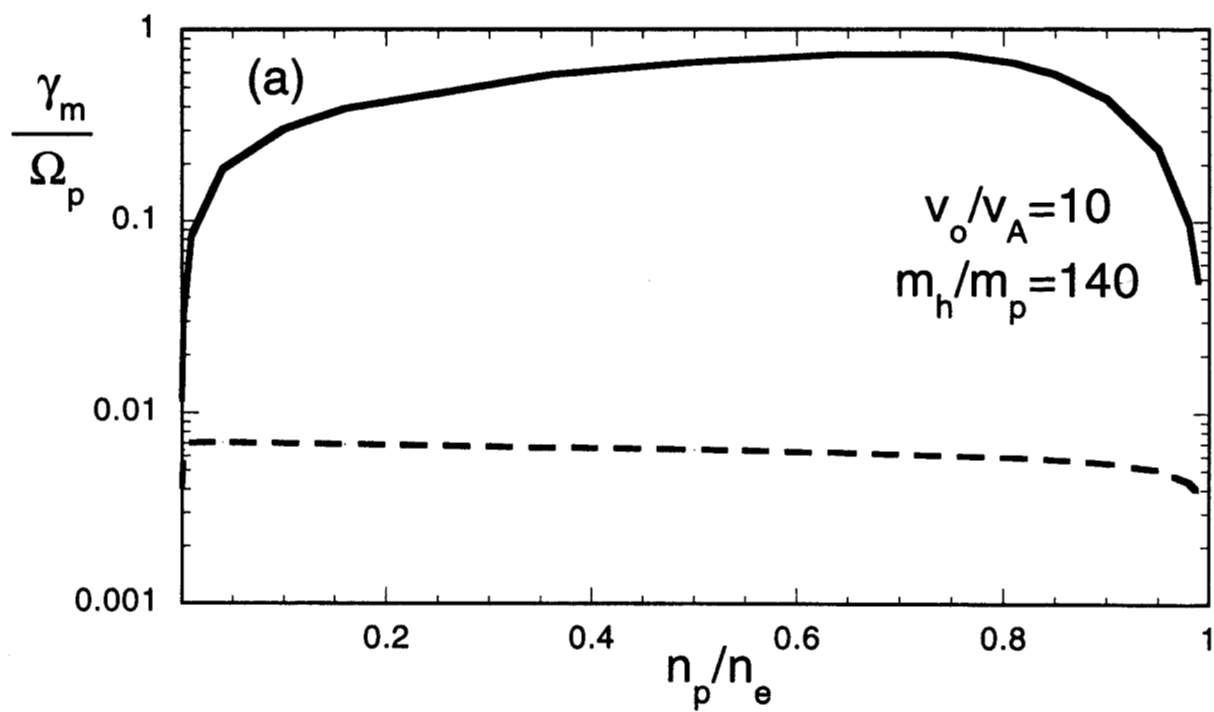


Figure 1a

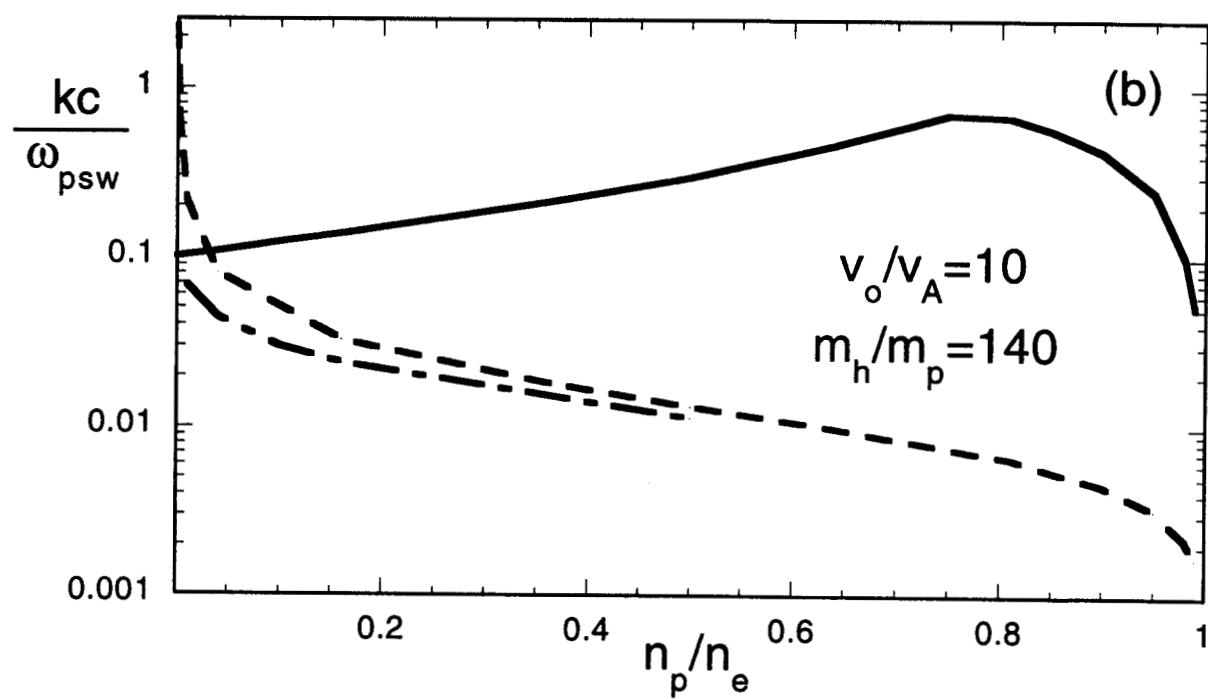


Figure 1b

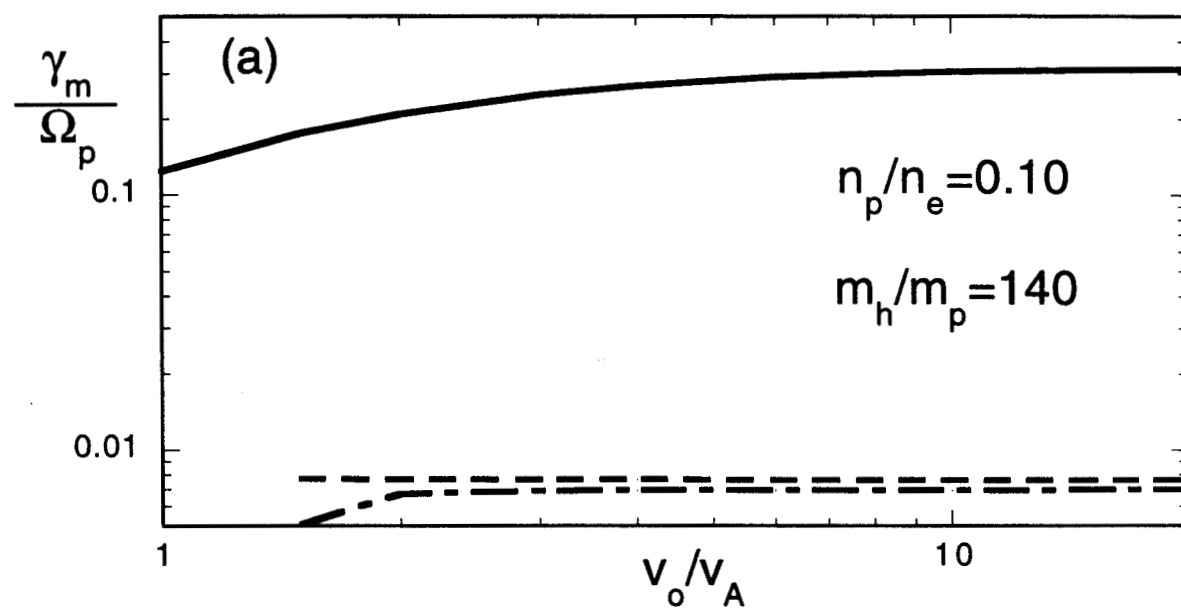


Figure 2a

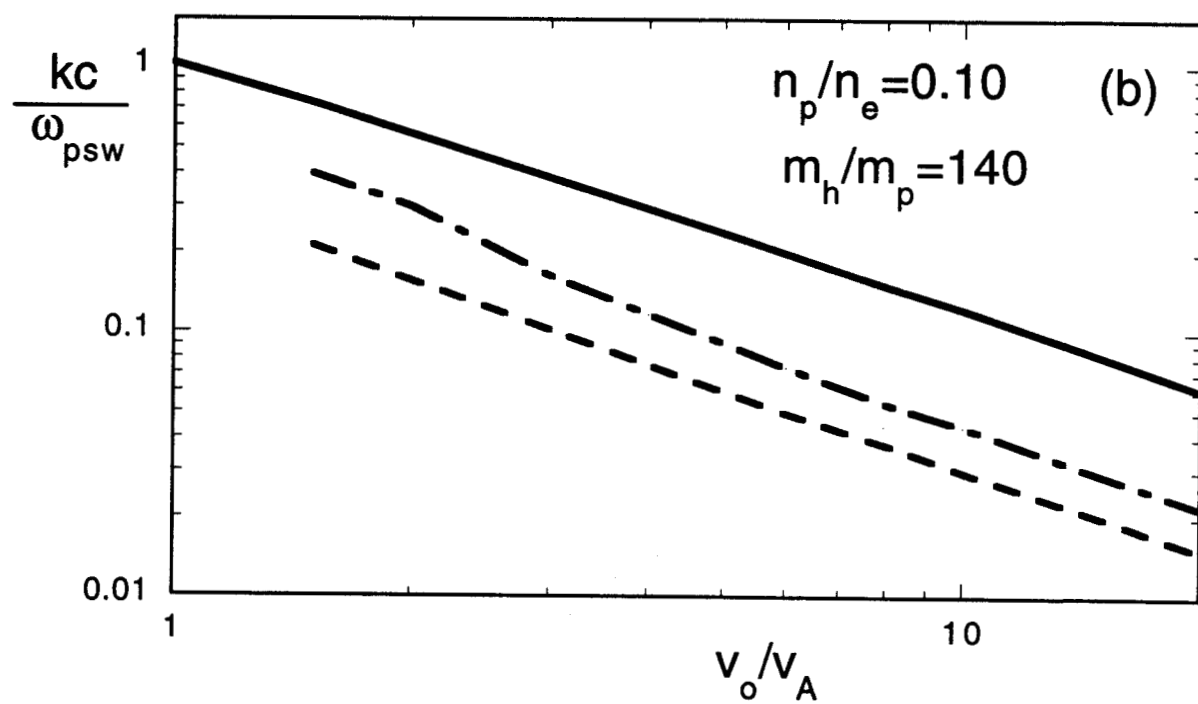


Figure 2b

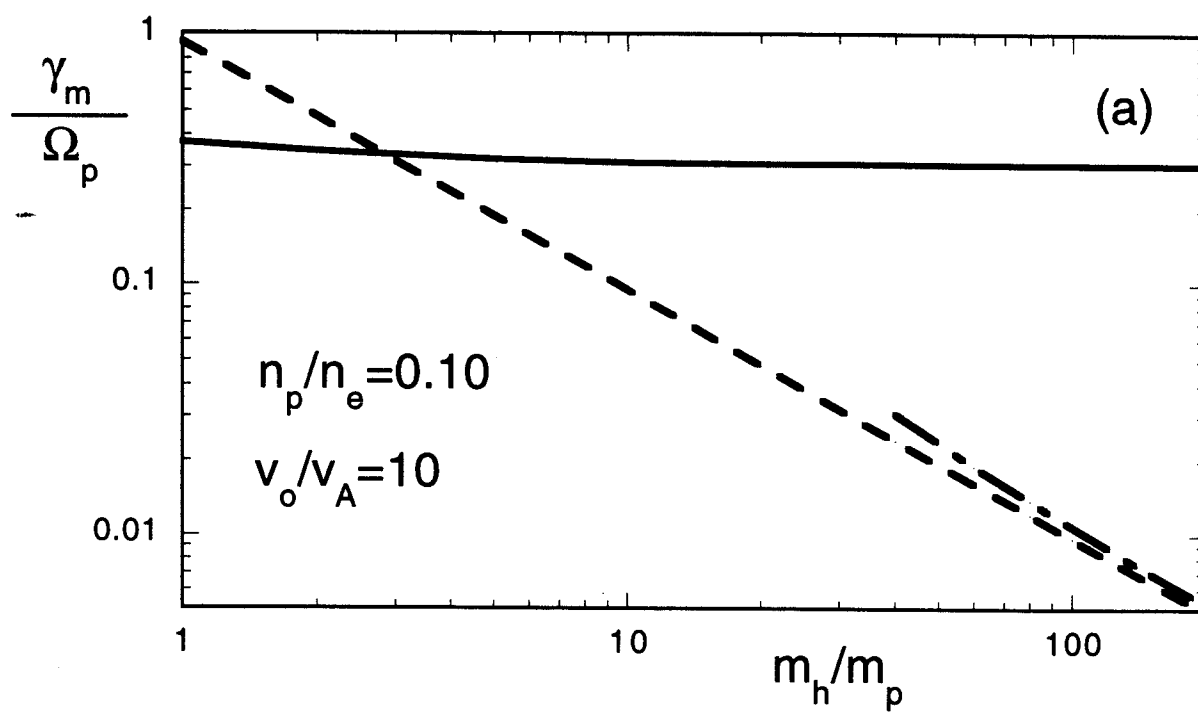


Figure 3a

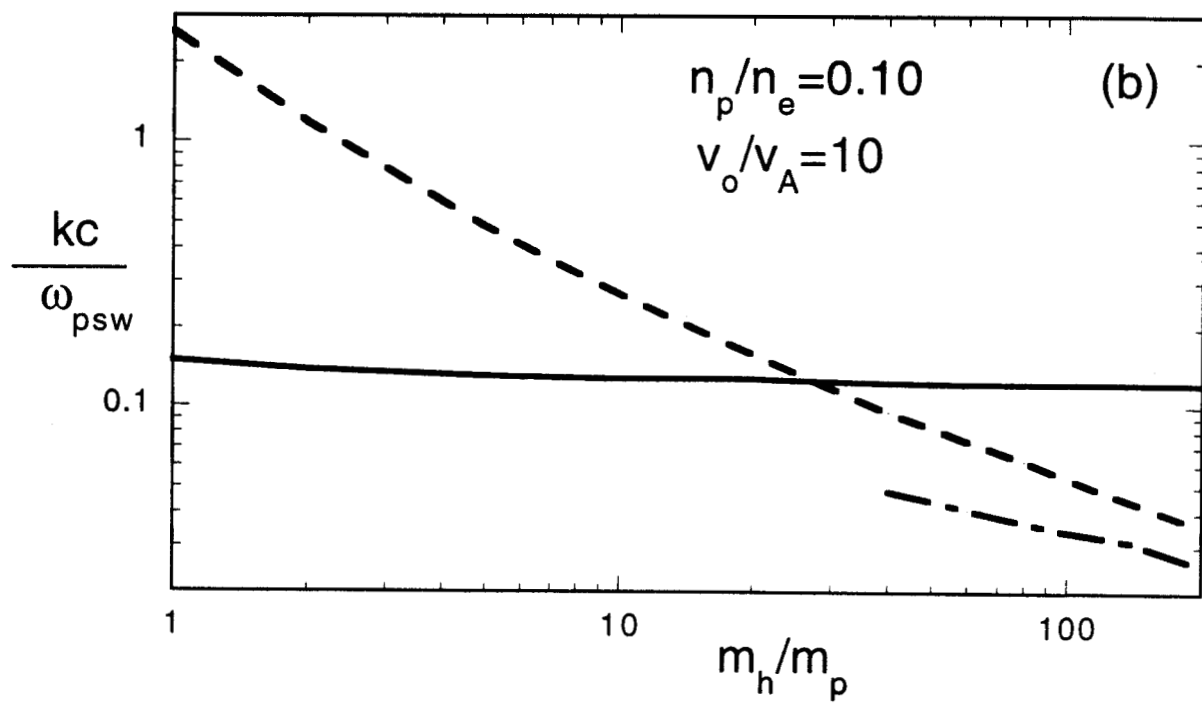


Figure 3b

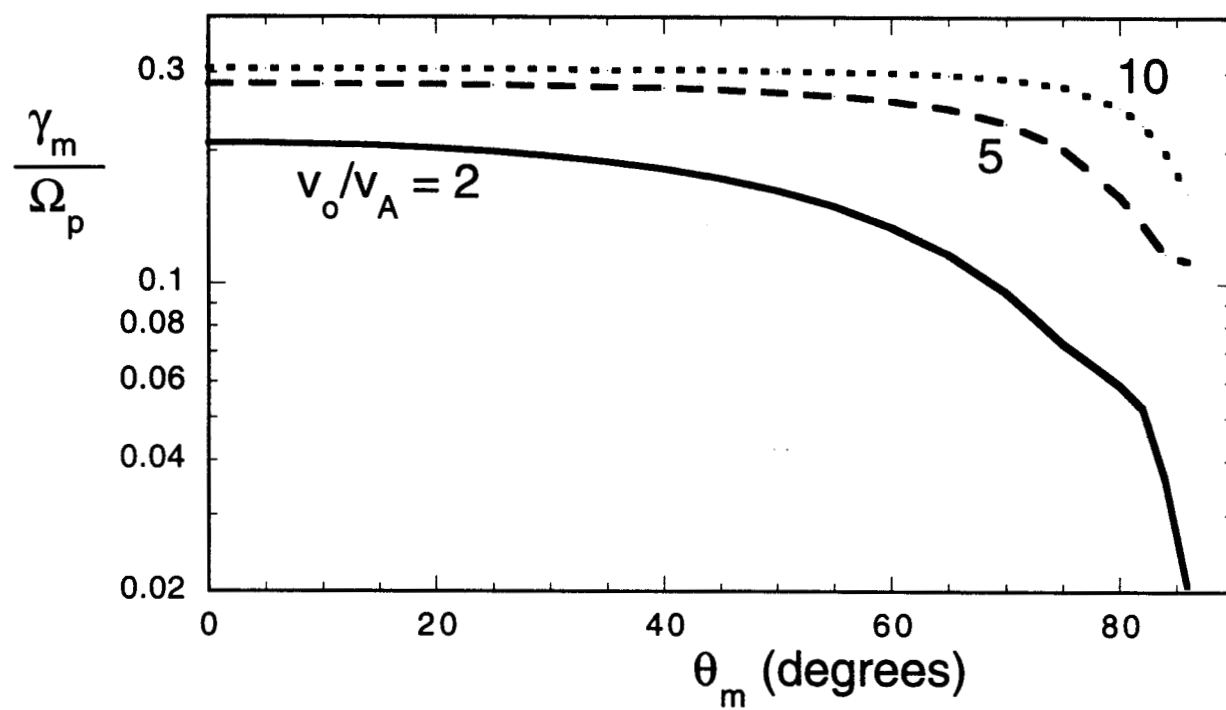


Figure 4

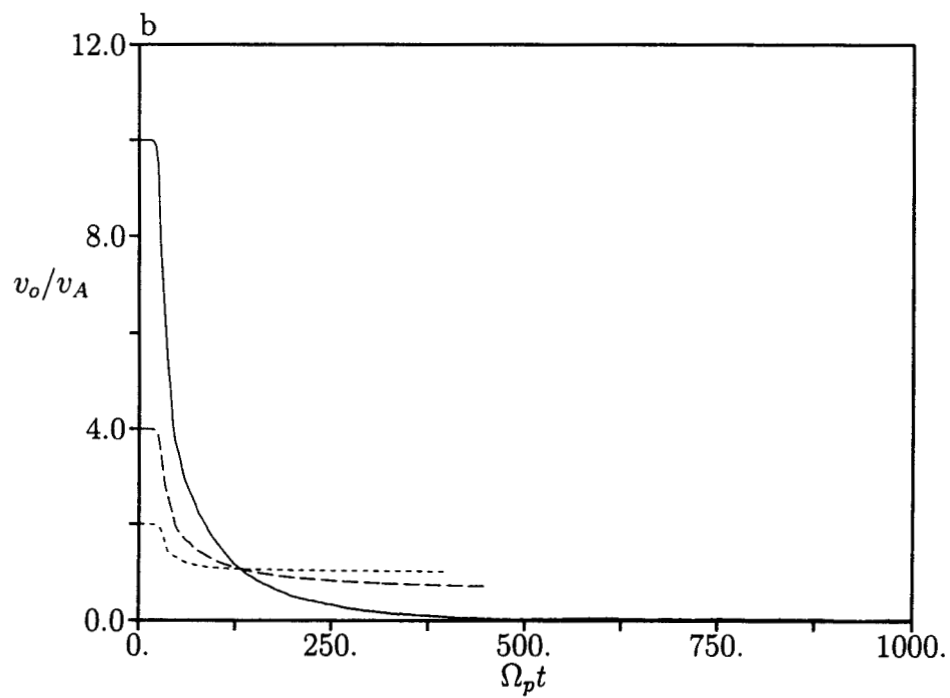
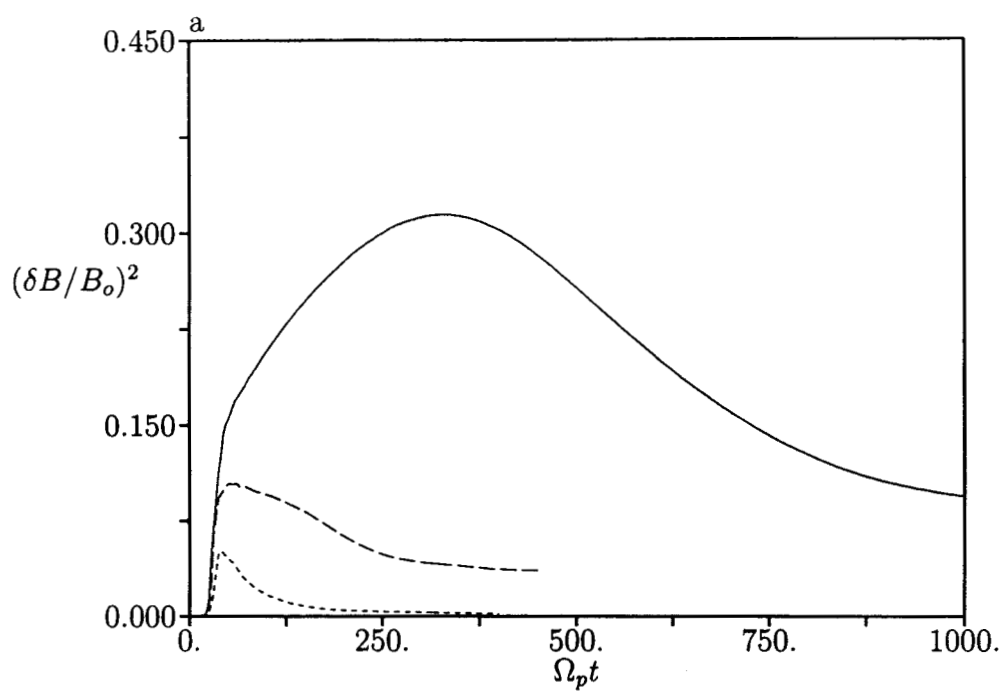


Figure 5

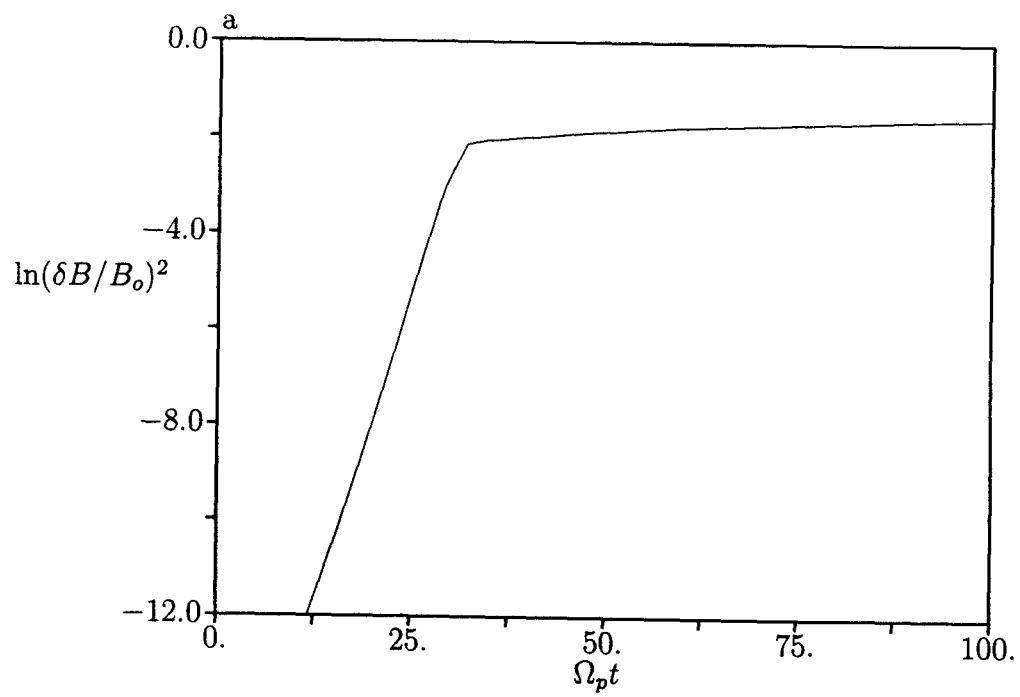


Figure 6

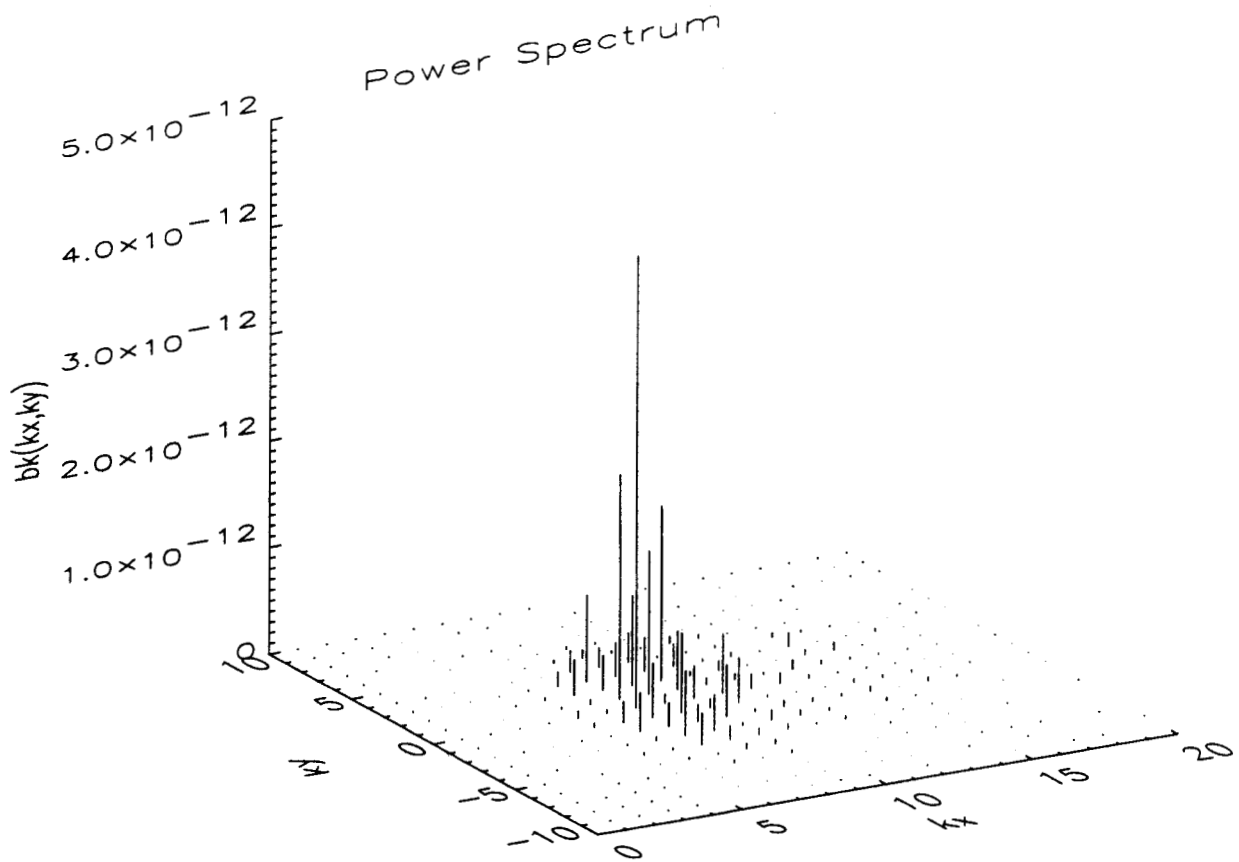


Fig 6b

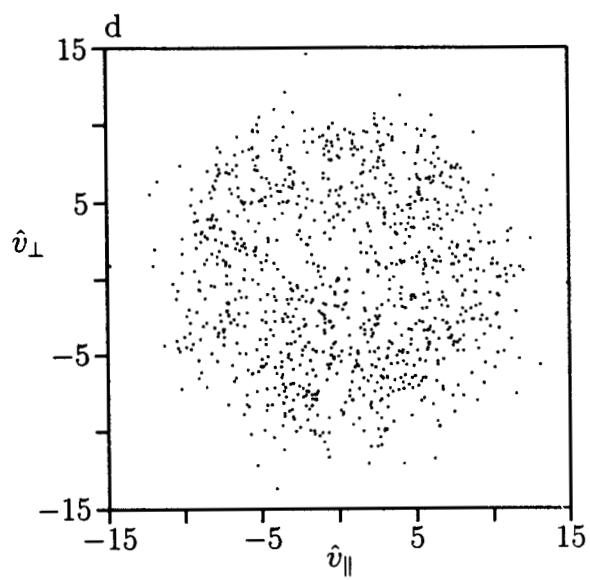
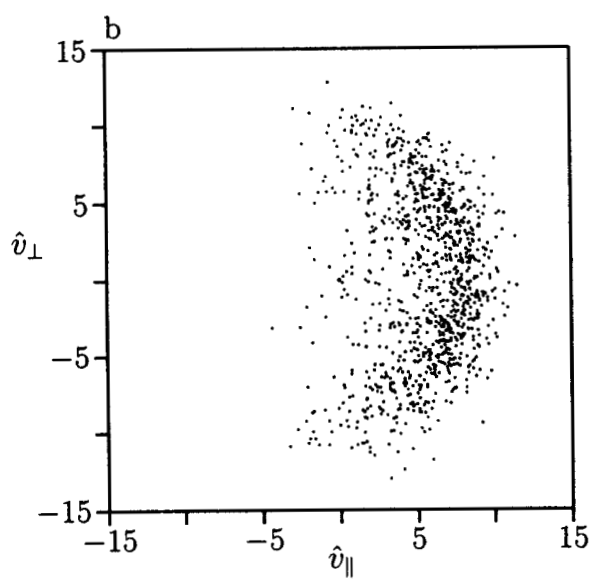
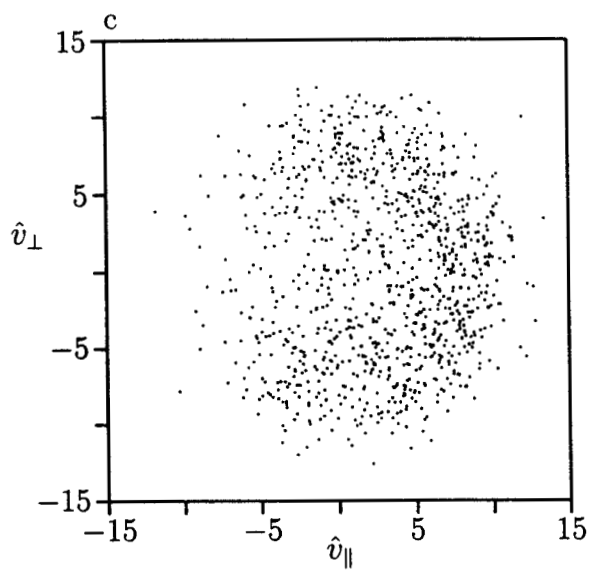
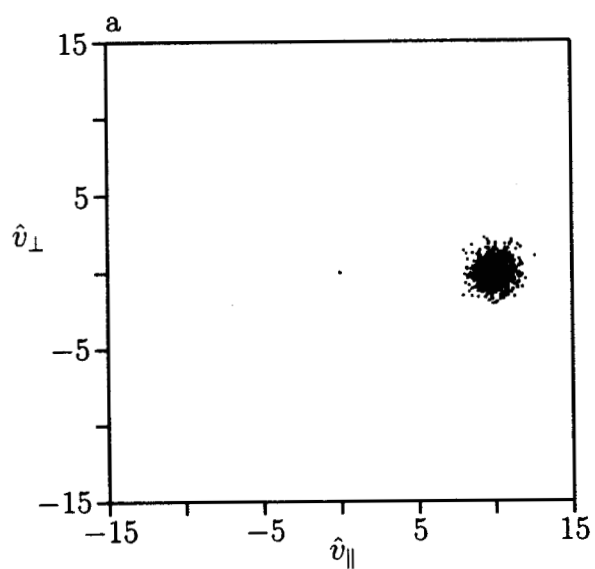


Figure 1

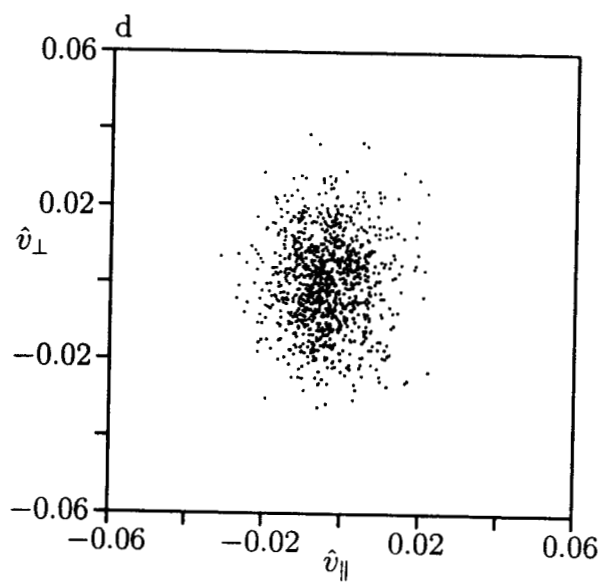
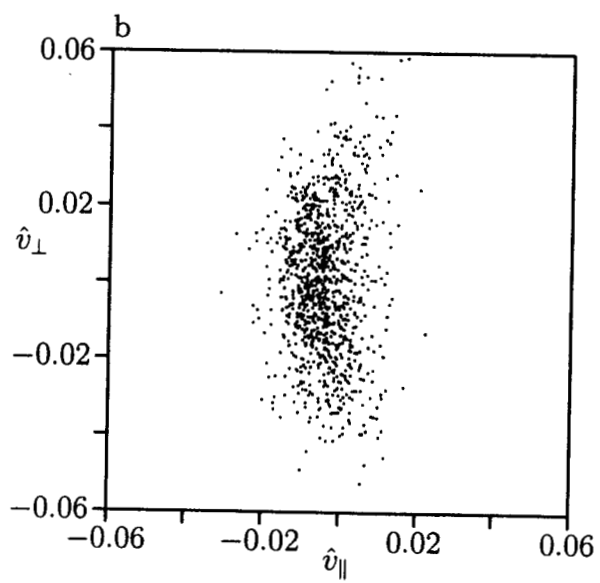
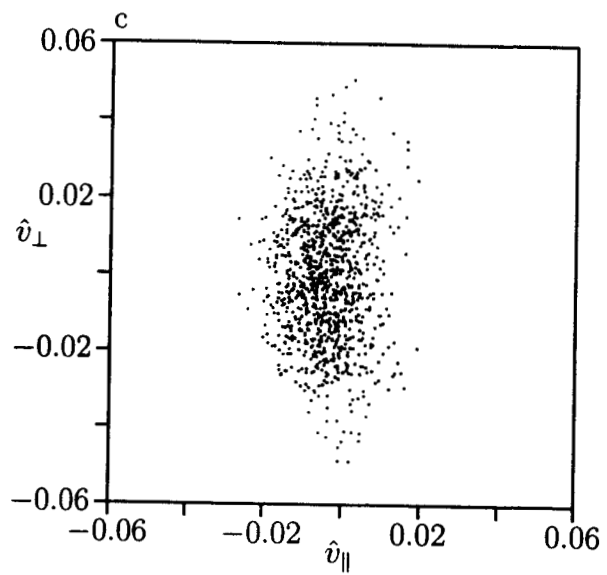
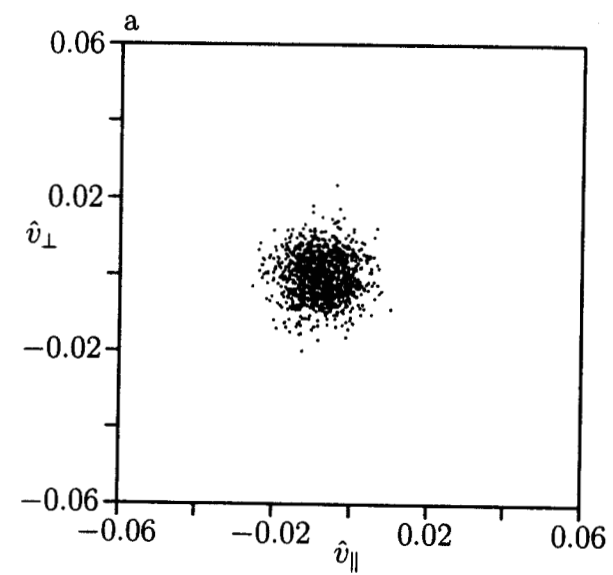


Figure 5

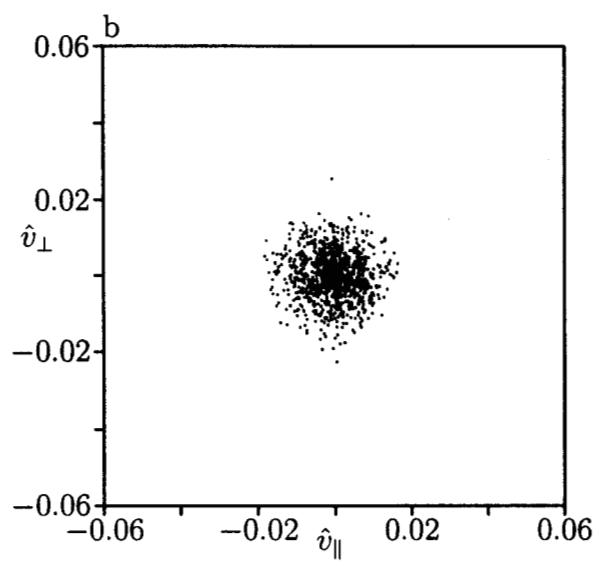
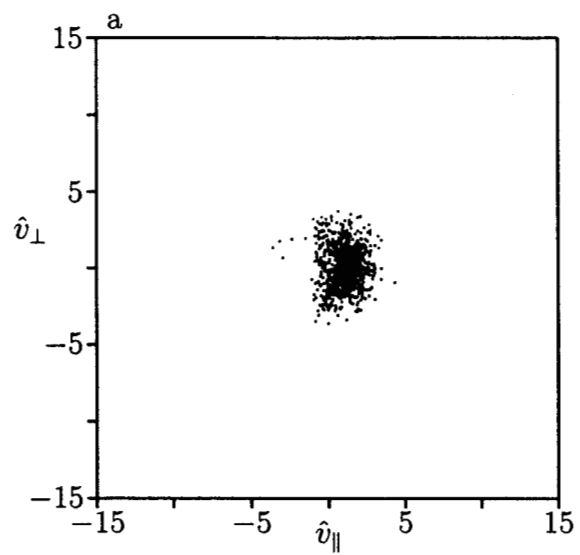


Figure 9

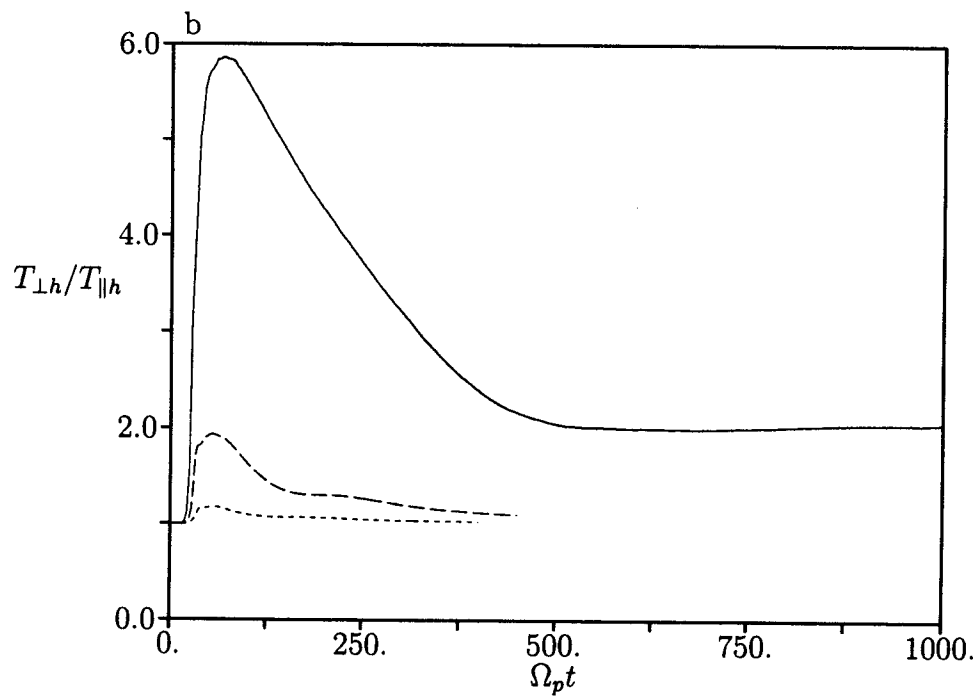
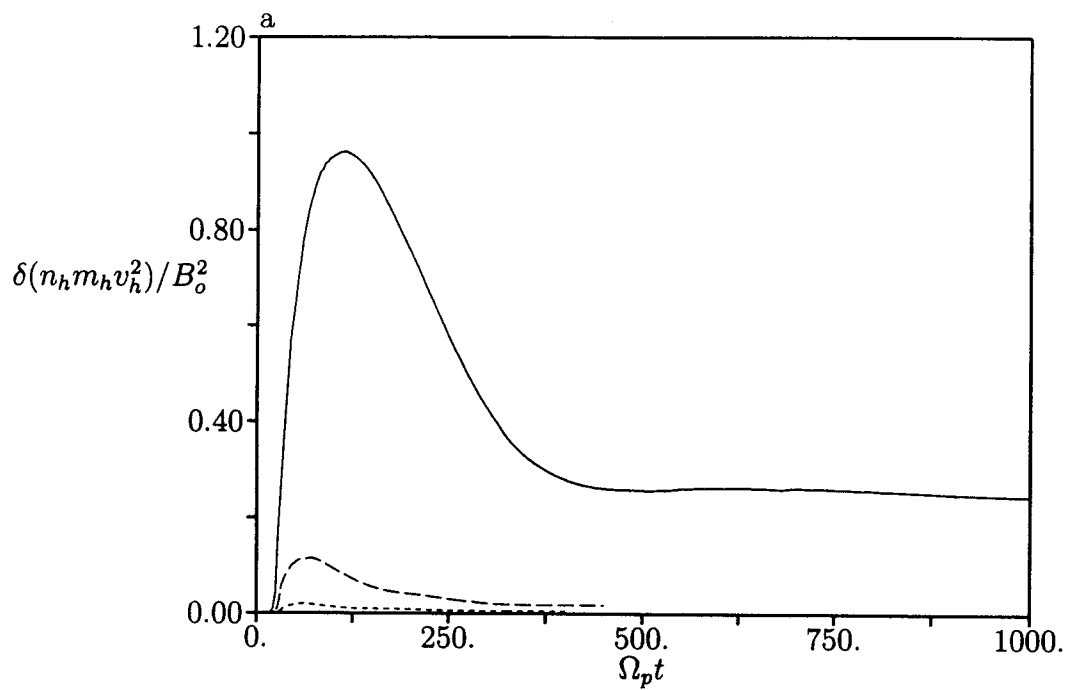


Figure 10

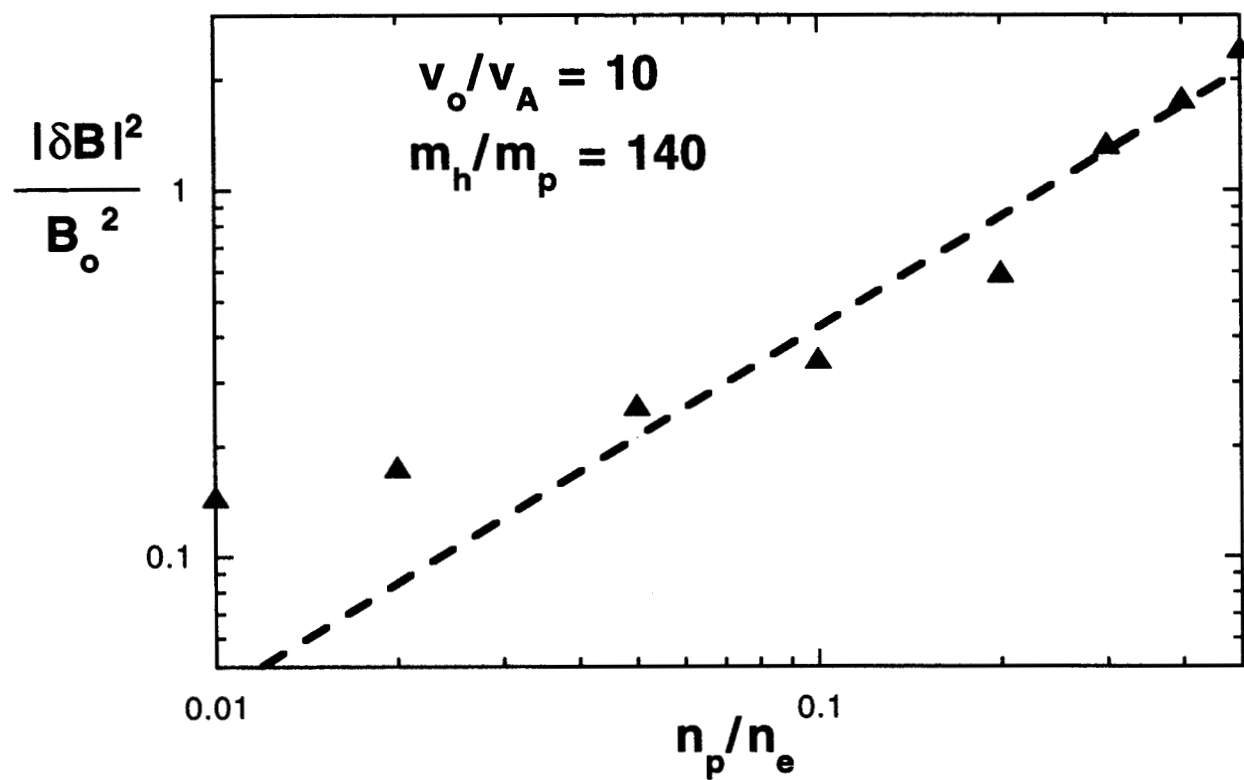


Figure 11

21 April 1999

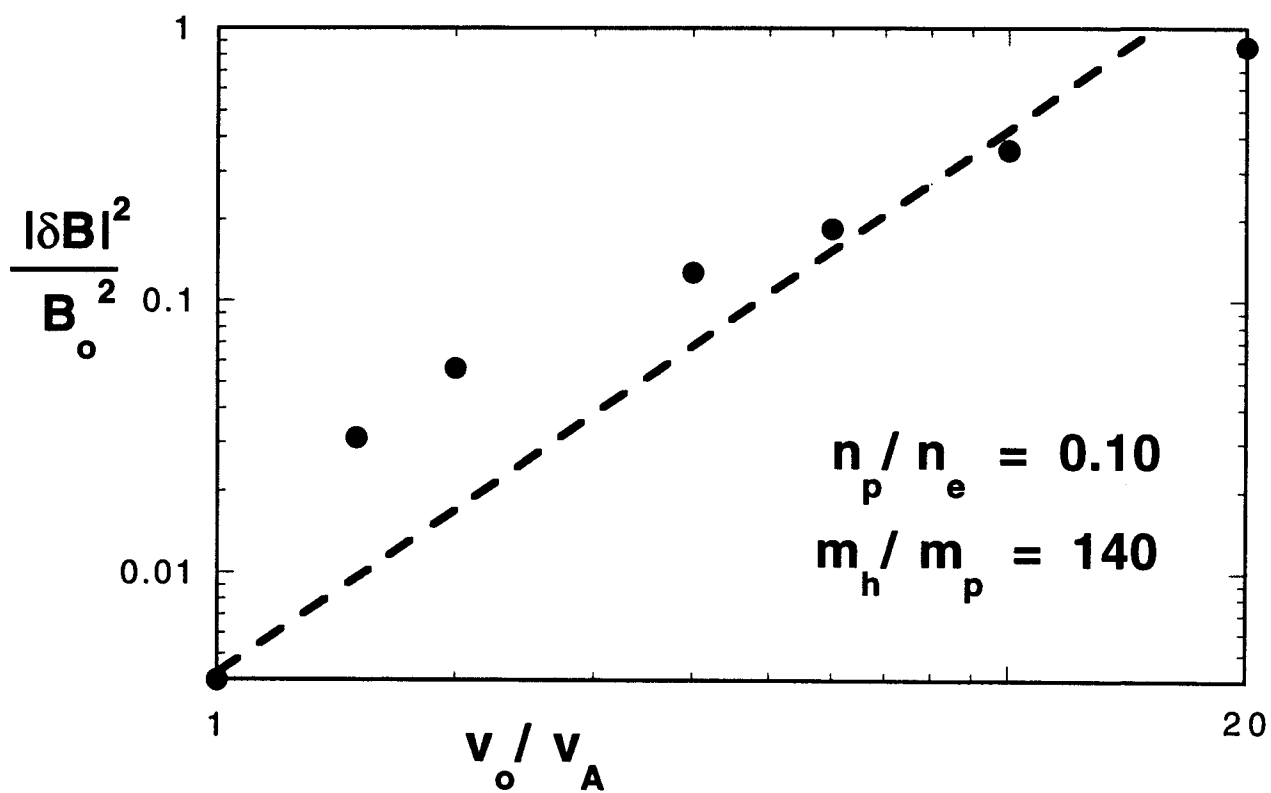


Figure 12

31 March 1999

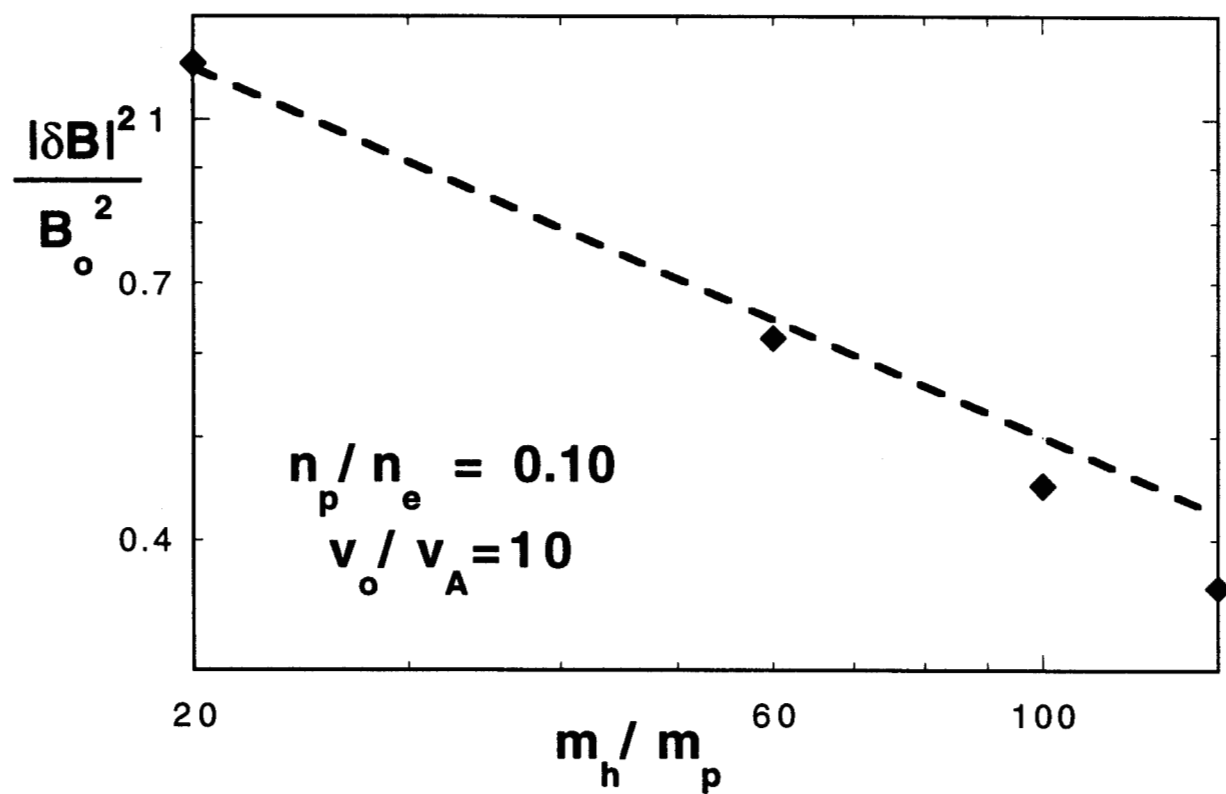


Figure 13

3 April 1999

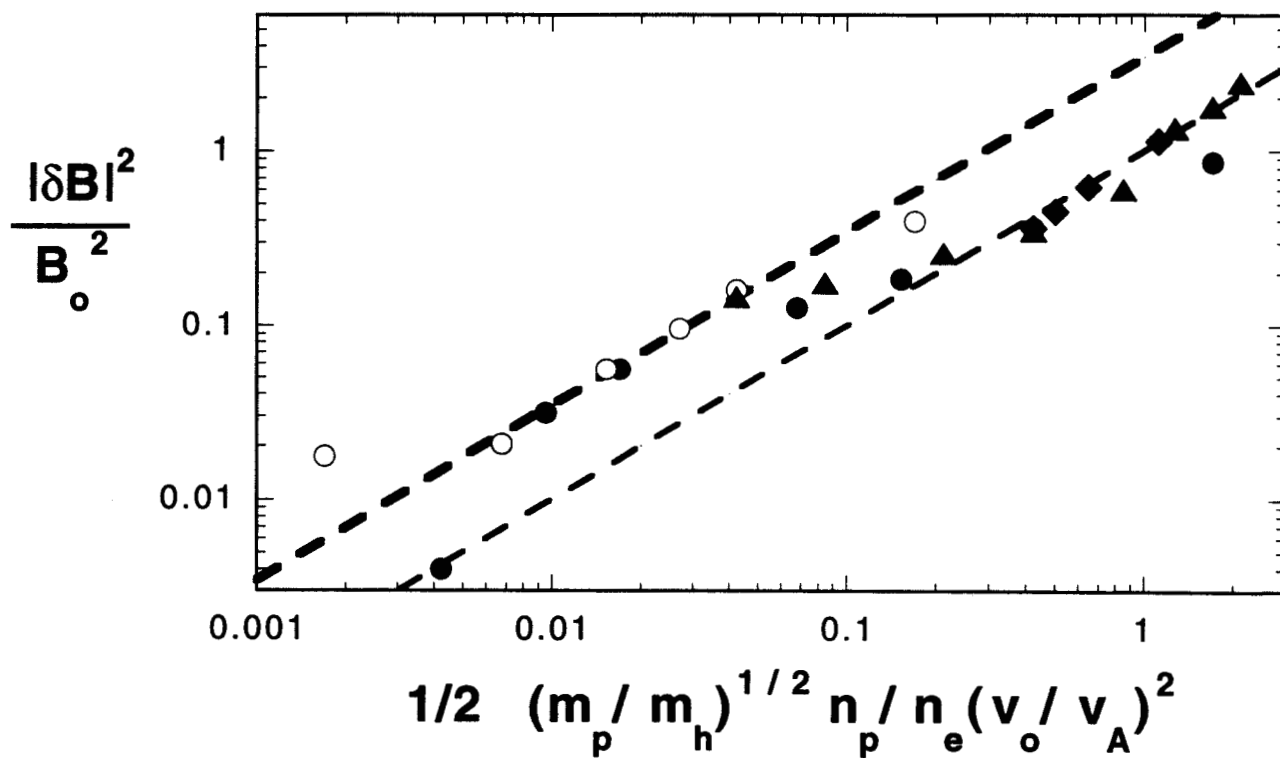


Figure 14

21 April 1999

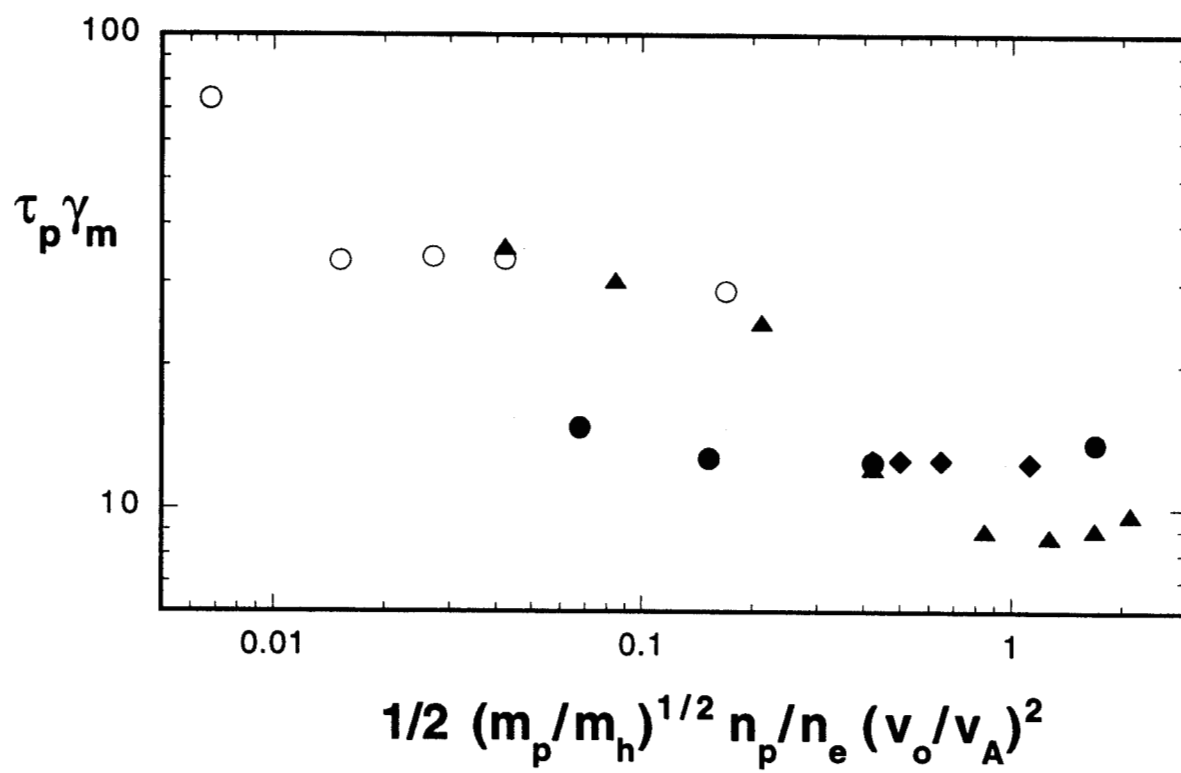


Figure 15